Optimized PET imaging for 4D treatment planning in radiotherapy: the virtual 4D PET strategy

Chiara Gianoli, PhD[1*], Marco Riboldi, PhD[1,2], Giulia Fontana MSc[1], Maria Grazia Giri, MSc[3], Daniela Grigolato, MD[4], Marco Ferdeghini, MD[4], Carlo Cavedon, PhD[3], Guido Baroni, PhD[1,2]

1. Dipartimento di Elettronica, Informazione e Bioingegneria (DEIB), Politecnico di Milano, Milano, Italy
2. Bioengineering Unit, Fondazione CNAO, Pavia, Italy
3. Medical Physics Unit, Azienda Ospedaliera Universitaria Integrata, Verona, Italy
4. Nuclear Medicine Unit, Azienda Ospedaliera Universitaria Integrata, Verona, Italy

Author for correspondence:

*Chiara Gianoli, PhD
Dipartimento di Elettronica, Informazione e Bioingegneria (DEIB)
Politecnico di Milano
P.za Leonardo da Vinci, 32
20133 Milano - IT
Tel. : +39-02-2399-9022
Fax : +39-02-2399-9000
E-Mail : chiara.gianoli@mail.polimi.it

Key words: 4D PET count statistics optimization, 4D CT motion modeling, 4D CT-PET, radiation oncology

30   *Running Title*: The *virtual 4D PET* strategy

Abbreviations: PET (Positron Emission Tomography), CT (Computed tomography), NCAT phantom (Nurbs-based CArdiac Torso phantom), TBR (Tumor to Background Ratio), MLEM (Maximum Likelihood Expectation Maximization reconstruction algorithm), OSEM (Ordered Subsets Maximum Likelihood Expectation Maximization)

40

50

Abstract

The purpose of the study is to evaluate the performance of a novel strategy, referred to as "*virtual 4D PET*", aiming at the optimization of hybrid 4D CT-PET scan for radiotherapy treatment planning. The *virtual 4D PET* strategy applies 4D CT motion modeling to avoid time-resolved PET image acquisition. This leads to a reduction of radioactive tracer administered to the patient and to a total acquisition time comparable to free-breathing PET studies.

60 The proposed method exploits a motion model derived from 4D CT, which is applied to the free-breathing PET to recover respiratory motion and motion blur. The free-breathing PET is warped according to the motion model, in order to generate the *virtual 4D PET*. The *virtual 4D PET* strategy was tested on images obtained from a 4D computational anthropomorphic phantom. The performance was compared to conventional motion compensated 4D PET. Tests were also carried out on clinical 4D CT-PET scans coming from seven lung and liver cancer patients.

The *virtual 4D PET* strategy was able to recover lesion motion, with comparable performance with respect to the motion compensated 4D PET.
70 The compensation of the activity blurring due to motion was successfully achieved in terms of spill out removal. Specific limitations were highlighted in terms of partial volume compensation. Results on clinical 4D CT-PET

scans confirmed the efficacy in 4D PET count statistics optimization, as equal to the free-breathing PET, and recovery of lesion motion.

Compared to conventional motion compensation strategies that explicitly require 4D PET imaging, the *virtual 4D PET* strategy reduces clinical workload and computational costs, resulting in significant advantages for radiotherapy treatment planning.

80

90

Introduction

Four-dimensional Positron Emission Tomography (4D PET) effectively accounts for the motion blur due to breathing (*1,2*). Nonetheless, the number of breathing phases in 4D PET is limited by the low count statistics, which has a negative impact on the signal to noise ratio (SNR) (*3*). The problem of 4D PET low count statistics has been tackled with the application of motion models, aiming at the reconstruction of motion compensated 4D PET images (*1*).

Different approaches to respiratory motion modeling have been proposed (*4*). In the following, we consider only those that describe a deformable motion model, accounting for the elastic nature of tissue deformation during breathing (*5*).

In some cases, these approaches rely on the estimation of motion models directly from the 4D PET dataset. Such models are therefore affected by the high noise and low spatial resolution typical of PET imaging. One possible approach is to estimate the 4D PET motion model during the PET image reconstruction process. Blume et al. (2010) proposed the inclusion of breathing deformation within the optimization function used for image reconstruction. They obtained a whole count statistics reconstruction of a motion compensated PET image, integrating all the 4D PET phases (*6*). Alternatively, the motion model is estimated from the 4D PET following the image reconstruction process. Some authors

implemented motion model estimation at the image resolution relying on deformable registration algorithms (*7,8,9*). Wallach et al. (2012) estimated the unknown "super resolution" reference image according to a maximum a posteriori (MAP) algorithm by modeling (i) the effect of motion, (ii) the spatial resolution blur and (iii) the effect of noise (*9*).

Conversely, a motion model based on 4D Computed Tomography (4D CT) can be applied, assuming ideal phase per phase co-registration between PET and CT images. The assumption is realistic when a hybrid 4D CT-PET scanner is available, providing consistent anatomo-functional volumes in the same imaging session (*10*). The 4D CT motion model estimation typically relies on image deformable registration methods (*11,12,13,14*). Models have been validated in 4D CT, showing that the accuracy is intrinsically dependent on the performance of the applied deformable registration method (*14*). However, one must be aware that any breathing pattern change between the two scans potentially compromises the reliability of the motion model, and therefore the accuracy of 4D PET count statistics optimization (*4*).

The state-of-the-art motion compensated 4D PET strategy based on 4D CT modeling is the 4D Maximum Likelihood Expectation Maximization reconstruction algorithm (MLEM), where the warping of PET images is embedded in the reconstruction process (*11,12,15*). This strategy uses all the acquired 4D PET phases to generate a motion compensated reference image

(intra-reconstruction warping). The reconstruction process requires the 4D CT deformation fields, which express both the direct and the inverse deformation between each 4D PET phase and the selected reference phase.

In this paper, we propose an alternative strategy ("*virtual 4D PET*") for time-resolved PET imaging, based on a 4D CT motion model, aiming at the optimization of 4D PET count statistics as equal to the free-breathing PET, in hybrid 4D CT-PET scanning (*16,17*). The 4D CT motion model is obtained by deformable image registration of 4D CT phases with a free breathing scan, thus representing the combined effects of respiratory motion and motion blur. The motion model is applied for the generation of an optimized 4D PET, starting from a whole count statistics 3D PET (i.e. the free-breathing PET), without requiring the acquisition of a 4D PET dataset. The comparative assessment of the proposed method, with respect to conventional motion compensated 4D PET (*1*), was performed considering that the challenge to recover the 4D PET dataset starting from free-breathing 3D PET entails potentially important advantages. The absence of a 4D PET acquisition procedure leads in clinical practice to the possibility to reduce (i) the quantity of radioactive tracer administered to the patient and (ii) the overall acquisition time. Furthermore, the *virtual* PET strategy results in reduced computational costs and lower CT-PET co-registration restrictiveness, as it is limited to average data over the breathing cycle. These peculiarities may result particularly valuable in the planning of

radiotherapy treatments for moving targets, which requires 4D CT acquisition and time-resolved PET imaging for more accurate target volume identification (*18*).

160

Materials and Methods

In the following paragraphs, the *virtual 4D PET* strategy is described and methodological differences with respect to conventional motion compensated 4D PET are highlighted. The 4D CT-PET NCAT (Nurbs-based CArdiac Torso) phantom (*19*) was applied for comparative testing in a computational simulation environment. Data coming from seven lung and liver cancer patients, who underwent 4D CT-PET imaging for radiotherapy treatment planning, was used for further assessment of the proposed method

170 on a clinical dataset.

Motion compensation in 4D PET based on 4D CT motion modeling

Deformable image registration was applied to register the available 4D CT dataset, accounting for the elastic nature of tissue deformation along the breathing cycle. Such information was codified as a set of deformation fields, expressing amount and direction of breathing motion in

8

correspondence of each voxel, as a function of the respiratory phase. The

180   open source software package "Plastimatch" was used to implement a B-spline based deformable registration method (*20*). The parameters of the registration procedure were refined on the NCAT phantom and maintained for patient data registration. Four multi-resolution stages of B-spline deformable registration were applied, based on root mean square error optimization. The sequence of stages featured decreasing grid spacing and increasing space resolution and number of iterations, as reported in Table I.

TABLE I

190   **Motion model definition**

The motion model resulting from 4D CT deformable image registration was used to warp the PET dataset and generate a whole count statistics optimized 4D PET. For patient data, the CT image grid resolution was maintained when warping PET images. This allowed us preserving the high resolution information provided by CT images, but required a sub-sampling of the warped PET images to recover the original voxel size.

With reference to Figure 1, the workflow for *virtual 4D PET* generation, compared to conventional motion compensated 4D PET, is

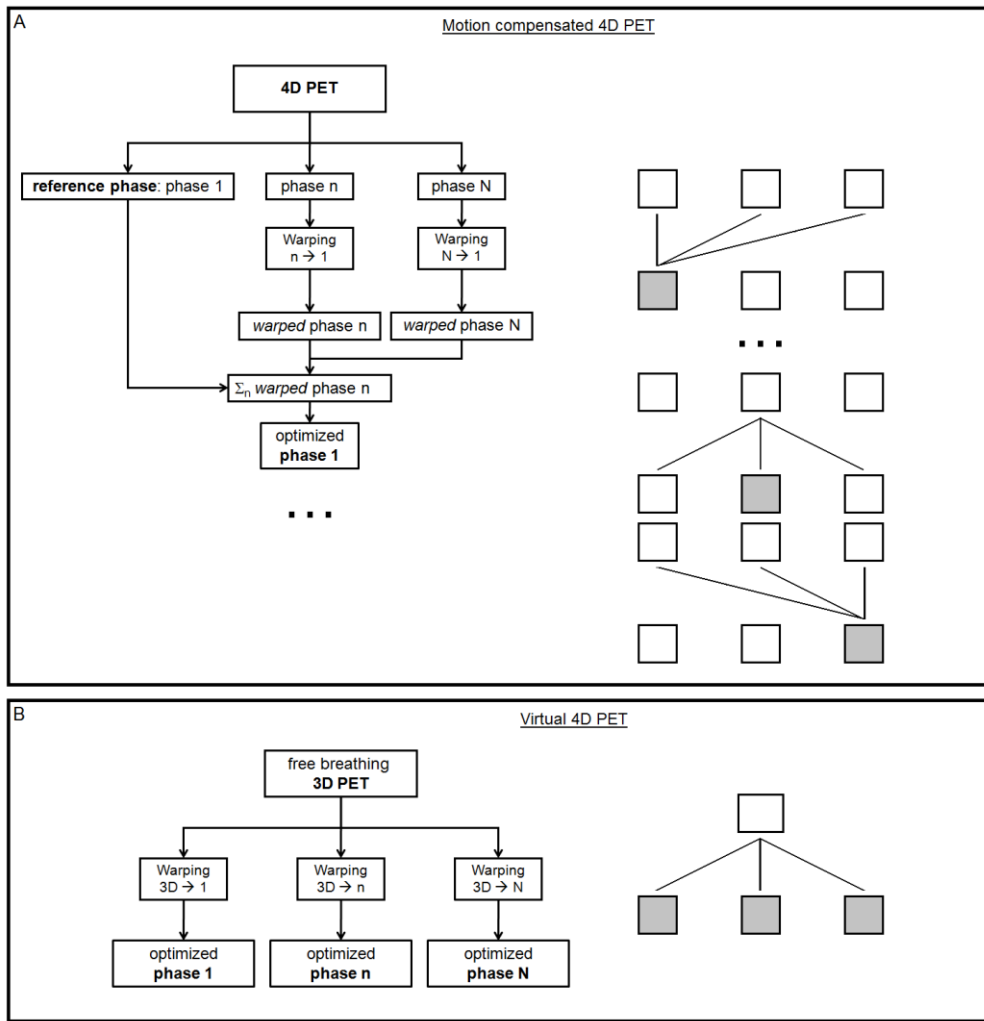200   described in the following paragraphs.

FIGURE 1. Motion compensated 4D PET (A) and *virtual 4D PET* (B) flowchart. The strategy complexity is exemplified on the right of the corresponding flowchart: the image registration steps needed to calculate the optimized 4D PET phases (gray boxes) are shown as connecting lines.

Virtual 4D PET

In the *virtual 4D PET* strategy, the motion model is defined by registering a phase-averaged 4D CT onto each phase of the 4D CT dataset. This is meant to include in the 4D CT motion model the combined effects of breathing motion and motion blur. The motion model is described by N registration steps, where N is the number of breathing phases. The phase-averaged 4D CT, and the corresponding phase-summed 4D PET, will be referred to in the following as 3D CT and 3D PET, respectively. In this strategy, the count statistics is optimized "a priori" with respect to the actual

220   motion model application. The *virtual 4D PET* volumes are generated by warping the whole count statistics 3D PET according to the deformation fields defined in the motion model (Figure 1). Since the acquisition of PET images in 4D is not explicitly required, precise co-registration is needed only between the 3D CT and the 3D PET volumes.

Motion compensated 4D PET

The motion model is calculated by registering the 4D CT phases onto a reference phase, thus entailing (N-1) registration steps. The complete

230   process requires N × (N-1) registration steps, as all phases need to be taken as reference. In this case the 4D CT motion model describes breathing

motion between different phases, where motion blur effects are minimized. The motion compensated 4D PET phases are warped according to the corresponding (N-1) deformation fields, resulting in "a posteriori" count statistics optimization (Figure 1). The co-registration between 4D CT and 4D PET volumes is required on a phase by phase basis.

4D CT-PET datasets

240 **Computational anthropomorphic phantom**

The 4D CT-PET NCAT phantom (*19*) was used for the comparative assessment of *virtual 4D PET* vs. motion compensated 4D PET. Such a phantom provides a 4D CT-PET dataset in controlled motion conditions, featuring ideal co-registration of CT and PET images at each breathing phase. The main features of the NCAT dataset used for testing are summarized in Table II.

TABLE II

250

Relying on the software tools provided by the NCAT phantom, an isolated lesion (2 cm diameter) was placed into the right lung. The TBR (Tumor to Background Ratio) was set to 3.62 for CT images and to 18.75

12

for PET images, respectively. Specifically, the lesion activity was set to 75 counts/voxel, whereas the pulmonary background measured 4 counts/voxel.

Image processing implemented in Matlab (The Mathworks Inc., Natick, MA, USA) was applied to the original 4D CT-PET NCAT volumes in order to obtain clinical-like images (Figure 2).

In order to simulate realistic 4D CT image quality, the NCAT 4DCT volumes underwent the following procedures:

- adding, slice by slice, of a Gaussian noise with mean value equal to the mean gray level of the slice and variance equal to 1% of the gray level variance;

- three-dimensional Gaussian filtering with standard deviation of 1.5 mm and size of the convolution kernel equal to $11 \times 11 \times 11$ voxel;

- rescaling of image gray levels to conventional CT Hounsfield Units (HU).

For the same reason, the NCAT 4DPET images were processed in the sinogram space as follows:

- slice by slice sinogram (i.e. direct sinogram) generation; the number of projections was fixed to 144 over a 180° range, resulting in a sinogram dimension of 256×144 (*21*). Each sinogram was scaled to account for the contribution of each slice to the total volume counts (set at 2×10^7);

13

- mono-dimensional Gaussian filtering of each projection (11×1 convolution kernel) with standard deviation of 2 mm, simulating the intrinsic physical resolution loss of a realistic PET scanner;

- adding of Poisson noise on sinograms with mean value equal to the sinogram pixel intensity;

280
- slice by slice iterative maximum likelihood reconstruction from projections according to the OSEM (Ordered Subsets Maximum Likelihood Expectation Maximization) algorithm, featuring 2 iterations and 8 subsets (*22*);

- rescaling of the reconstructed image in order to recover the initial image counts (2×10^7counts);

- two-dimensional Gaussian filtering of the reconstructed image (post-reconstruction filtering) with standard deviation of 4 mm and size of the convolution kernel of 11×11 pixel;

290
- three-dimensional Gaussian filtering applied to the reconstructed volume, with standard deviation of 4 mm and size of the convolution kernel of 11×11×11 voxel; such a procedure enhanced the smoothness of reconstructed data and conferred continuity between adjacent slices.

The generation of 3D CT and 3D PET images, which is necessary for the implementation of the *virtual 4D PET* strategy, was performed by

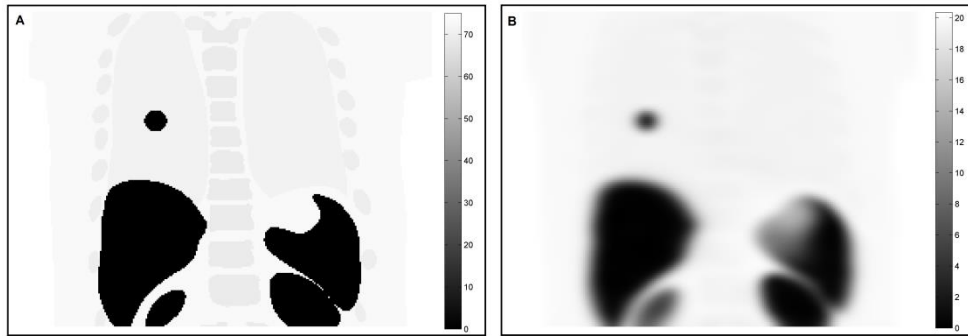averaging and summing the processed 4D CT and 4D PET volumes, respectively.

FIGURE 2. Coronal slices displaying the lesion for the original NCAT volume (A) and the clinical-like corresponding image (B) for PET. The different color bars indicate the counts scaling applied to the original NCAT volume.

Patient data

Clinical data were collected from seven patients, who underwent 4D CT-PET hybrid acquisition on a GEMINI TF Big Bore PET/CT (Philips Medical Systems, Eindhoven, The Netherlands). Respiratory motion was monitored through the Real-time Position Management system (RPM, Varian Medical Systems, Palo Alto, CA). The 4D CT-PET volumes were sorted into 4 breathing phases according to a phase-based binning protocol. The scanner performed attenuation and scatter corrected PET reconstruction by means of the 3D RAMLA (Row Action Maximum Likelihood

Algorithm) algorithm (*23*). As for the NCAT phantom data, the generation of artificial 3D CT and 3D PET was performed by averaging the 4D CT and 4D PET volumes, respectively.

The related image and clinical features for the patient study are summarized in Table III.

320 TABLE III

Quantification of performance

Lesion segmentation

Validation procedure was focused on the extraction of lesion geometrical features (position and volume), which required the definition of a specific method for lesion segmentation. This is in agreement with the envisioned clinical application in radiotherapy treatment planning (*24*) of
330 moving lesions due to respiration.

For the NCAT phantom the ground truth lesion segmentation was available and identical for CT and PET images. In order to assess the lesion quantification on warped images, a threshold segmentation was implemented within the lesion VOI (Volume of Interest). The initialization threshold level was set at 50% of the range defined by the maximum

16

intensity value in the lesion. The mean intensity value of the pulmonary background region was defined as 50% of the measured TBR. The optimal threshold level was tuned by means of an automatic procedure based on volume quantification. The threshold level was iteratively adjusted until the

340   segmented volume fitted the ground truth segmentation (with a tolerance of ±10 voxels over a volume measuring 1517 voxels, corresponding to ±0.66%). The gray level step adopted to gradually modify the threshold value was set to 1 HU for CT (0.05% of the full scale range) and 0.05 counts for PET (0.25% of the full range). This is consistent with the TBR, as the value for PET is more than 5 times compared to CT (see the "Computational anthropomorphic phantom" paragraph in the "Materials and Methods" section).

For patient datasets, lesion identification was performed by means of threshold segmentation. In CT images, the threshold value adjustment was

350   supervised by a trained operator. When required, the operator contoured manually the lesion in order to achieve adequate separation from the chest wall or the diaphragm. A morphological closing operator was applied to the segmented lesions, in order to smooth contours. In PET images, the threshold level was fixed to 40% of the measured TBR (*25*).

A metric measuring the relative overlap between segmented structures was calculated, according to:

$$overlap = \frac{L_{ref} \cap L}{L_{ref}}\%$$

17

where L_{ref} is the lesion segmentation in the fixed image.

360   *Inter-modality quantification*

Inter-modality quantification was performed to verify the co-registration between CT and PET images. The analysis compared the lesion position in correspondence of the same breathing phase in the 4D CT and 4D PET images. In the patient datasets, the inter-modality quantification provided the relative lesion displacement throughout the 4D images sequence with respect to its average position. This allowed us to consider quantification criteria independent of co-registration errors between the CT and PET volumes.

370

Intra-modality quantification

Intra-modality quantification was performed both for CT and PET volumes, as a way to assess the 4D CT motion model and the corresponding PET warping. The availability of the original 4D PET images for comparison allowed us to evaluate (i) lesion motion and (ii) blur compensation in the generated *virtual 4D PET* images.

<u>Results</u>

Computational anthropomorphic phantom

In the NCAT phantom the exact correspondence between 4D CT and 4D PET volumes is available by construction. Also, ground truth segmentations were corresponding between 4D CT and 4D PET volumes by phantom design. Therefore, only the intra-modality quantification is reported.

390   *<u>Intra-modality quantification</u>*

Virtual 4D PET

Quantification was performed on the 10 breathing phases defined in the NCAT respiratory cycle. The aim of this quantification was to assess the level of similarity between lesion localization (centroid) and volume (overlap).

Figure 3 (A) reports the lesion centroid trajectory over the breathing cycle along the superior-inferior direction for the 4D PET and the *virtual 4D*

400   *PET* volumes. In order to quantify the effect of deformable registration errors, the Euclidean distances between lesion centroids obtained by

warping the average 3D CT on each phase of the 4D CT and the corresponding 4D CT phase were calculated. The mean error in centroid localization was 0.192 mm with a maximum of 0.339 mm in correspondence of the 20% phase. The same quantification on the *virtual 4D PET* resulted in a mean error of 0.370 mm and a maximum error of 0.623 mm in correspondence of the 20% phase, which was assessed to be considerably lower than the voxel size (1.5 mm). This was obtained in presence of a simulated lesion motion of approximately 9 mm peak to peak, which is depicted in Figure 3 (B). As a measure of the quality of the deformable registration procedure in the 4D CT motion model, the relative overlap between the segmented lesion volume on the 4D phases and the corresponding warped phases was calculated. The minimum relative overlap was equal to 94.0% for CT and 92.8% for PET, both in correspondence of the 70% phase. The mean relative overlap among the 10 phases was equal to 95.6% for CT and 94.2% for PET. Deviations from perfect overlap were due to inaccuracies at the edges of the segmented volume, due to voxel intensity modification introduced by image warping.
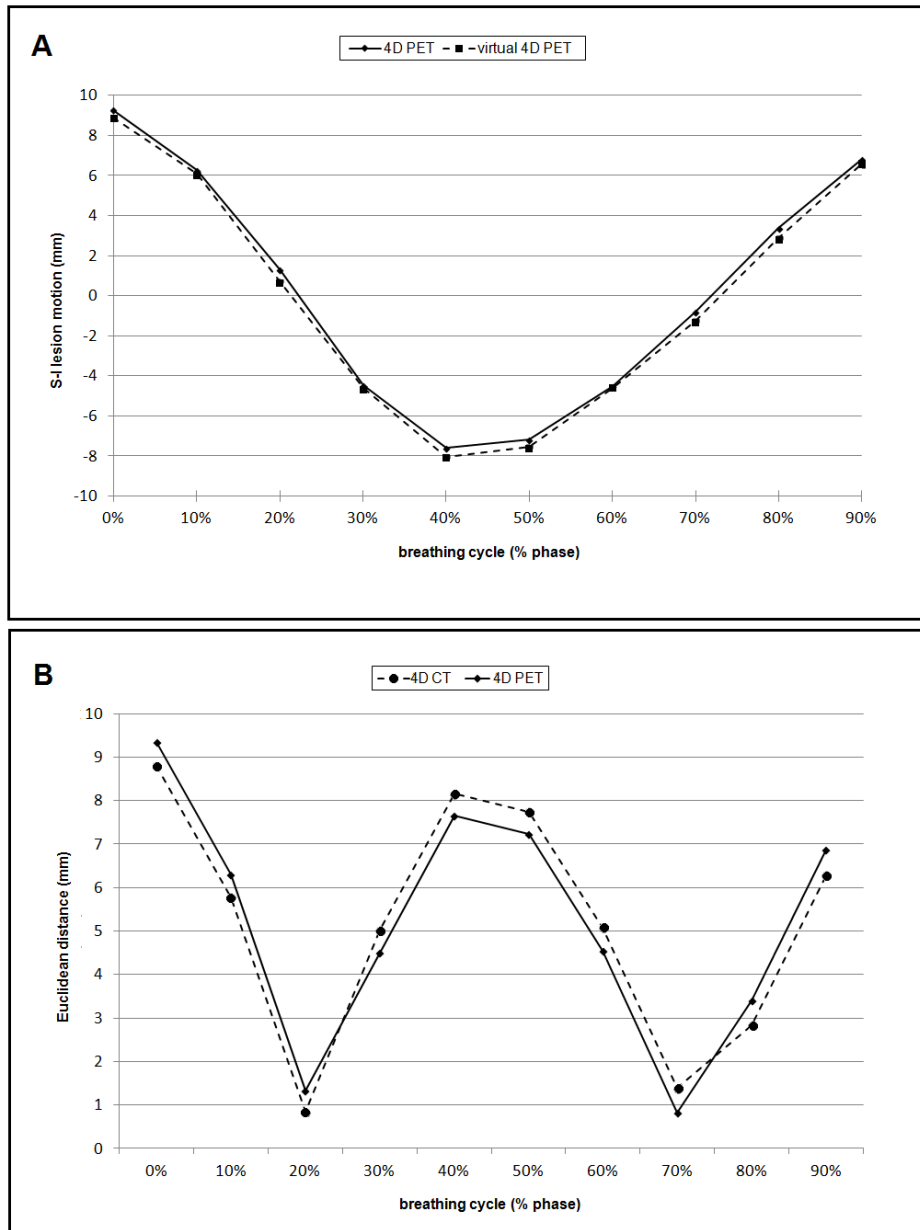
420

FIGURE 3. Lesion centroids trajectory in the superior-inferior direction (A). Euclidean distance between the lesion centroids of 4D phases and the averaged 3D volume, for CT and PET (B). The exhale peak corresponds to 0% of breathing cycle, the inhale peak corresponds to 50% of breathing cycle.

In order to assess the level of noise in the warped 4D PET, the voxel intensity variance in the pulmonary uniform background at the 0% phase was calculated, by segmenting the region on the corresponding original NCAT phantom. The *virtual* 4D PET resulted in a statistical noise variance of 0.58 counts^2 (vs. 0.97 counts^2 for the 4D PET).

Motion compensated 4D PET

The quantification was performed on a single reference phase. The phase corresponding to the exhale peak (the 0% phase) was selected. Such a choice accounts for the most challenging case in terms of 4D CT motion modeling, i.e. the peak to peak lesion excursion.

The Euclidean distances between lesion centroids of the 9 warped CT phases and the CT reference phase were calculated, in order to quantify the motion model error for each 4D CT contribution. The mean error resulted in 0.083 mm, with a maximum error of 0.137 mm in correspondence of the 50% phase, i.e. the inhale peak. The corresponding motion compensated 4D CT, resulting from average of the CT reference phase and the 9 warped CT phases, showed an error of 0.026 mm. The averaging among all contributions mitigated the registration error in the motion compensated 4D CT, resulting in accurate lesion segmentation. The same quantification was performed on 4D PET. The average motion model

22

error in PET measured 0.091 mm, with a maximum error of 0.172 mm in correspondence of the 50% phase. Similarly to what shown for 4D CT, the

450   motion compensated 4D PET showed an error of 0.049 mm.

The minimum lesion overlap over the breathing cycle was equal to 98.4% for CT and to 97.5% for PET (in correspondence of the 50% phase), whereas the mean overlap among the 9 phases measured 98.8% for CT and 98.2% for PET. The relative overlap between the segmented lesion volume on the reference phase and on the motion compensated phase resulted in 99.4% for CT and in 98.8% for PET.

The level of noise in the motion compensated 4D PET, calculated as described in the previous paragraph, resulted in 0.83 counts^2 (vs. 0.97 counts^2 for the 4D PET).

460

Virtual 4D PET vs. motion compensated 4D PET

For comparison purposes, Figure 4 reports the activity profiles in correspondence of the 3D PET lesion centroid and at the 0% phase in the 4D PET, the *virtual 4D PET* and motion compensated 4D PET. For reference, the original ideal activity profile generated in the NCAT phantom is reported. The maximum activity value of the *virtual 4D PET* is below the maximum activity value in the 4D PET, and is consistent with the maximum value in the 3D PET. However, the profile of the warped lesion shows that

23

470   the spill out activity (outside the lesion volume) is removed and that the

partial volume effect (inside the lesion volume) is partially compensated.
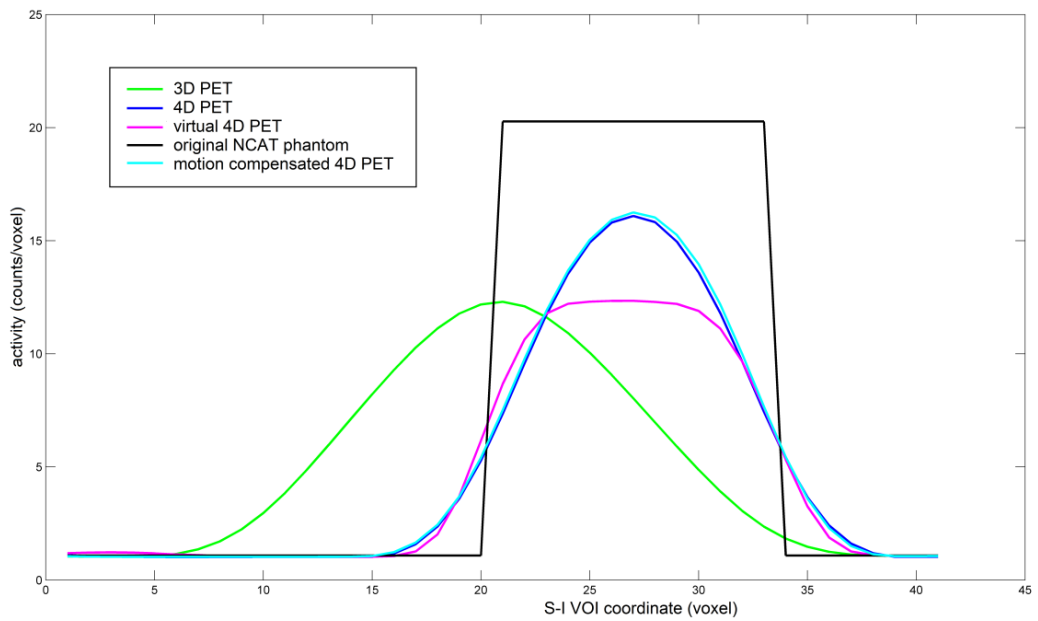
FIGURE 4. Lesion activity profiles along the superior-inferior coordinate of the 3D PET (green), the 4D PET (blue) and the *virtual 4D PET* (pink) and the original NCAT phantom (black) in correspondence of the 0% phase. The motion compensated 4D PET is displayed in light blue. The *virtual 4D PET*, the motion compensated 4D PET and 3D PET were scaled by a factor 10 to account for the different count statistics. The VOI was placed in

480   correspondence of the 3D PET lesion centroid.

Patient data

Inter-modality quantification

The size of lesion motion and the level of co-registration between real CT and PET images were quantified by calculating the Euclidean distance of segmented lesion centroids throughout the 4D image sequence, with respect to the average position. For Patient 1, Patient 4, Patient 6 and Patient 7 the displacement resulted negligible (lower than voxel size) and comparable for CT and PET. For such patients, the lesion in the upper part and in the posterior part of the lung (Table III) did not move appreciably with breathing, and the 4D CT and 4D PET phases resulted in stable co-registration. For Patient 2, Patient 3, and Patient 5 the lesion was in the abdominal area (Table III) and showed a different peak to peak range of motion when measured on CT and PET. This suggests the lack of co-registration between CT and PET, which may have been significantly influenced by the noise affecting clinical 4D PET images. Table IV summarizes the lesion range of motion.

TABLE IV

25

The co-registration inaccuracies resulted in 5.48 mm for Patient 2, 3.95 mm for Patient 3 and 3.77 mm for Patient 5, which is comparable to the PET voxel dimensions (Table III). For other patients the range of motion was limited and co-registration inaccuracies resulted always lower than PET voxel size.

510

Intra-modality quantification

Virtual 4D PET

Table V summarizes the lesion centroid localization error. The overall maximum errors were comparable to the PET voxel size and the CT slice thickness.

TABLE V

520

As an exemplifying case, Figure 5 reports the real 4D PET, the *virtual 4D PET* and the motion compensated 4D PET for Patient 2.

26
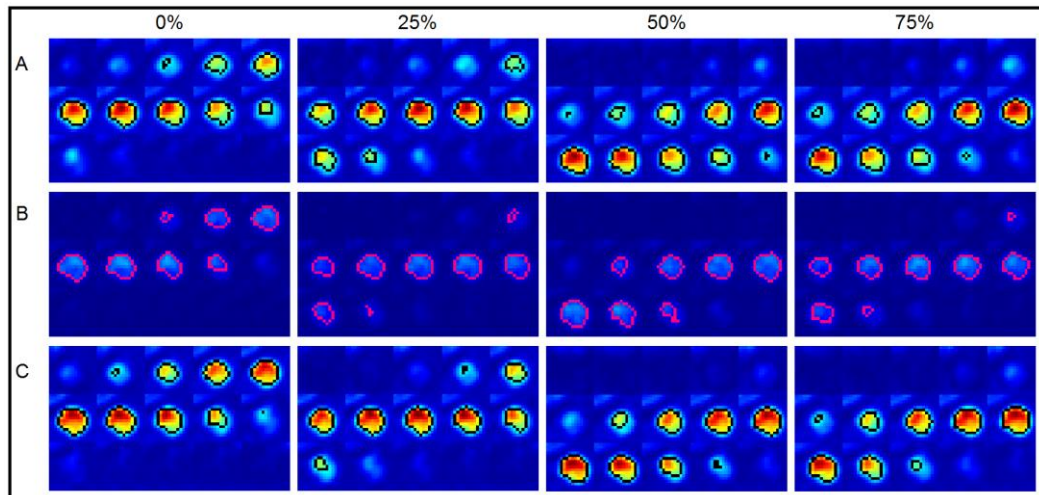
FIGURE 5. The *virtual 4D PET* (A), the 4D PET (B) and the motion compensated 4D PET (C) sequences describing the breathing cycle for the lesion in Patient 2. The inhale phase corresponds to 0% of breathing cycle, the exhale phase corresponds to 50% of breathing cycle (phase-based binning protocol).

530   The relative overlap was calculated between the segmented lesion volume on the real 4D PET and the corresponding *virtual 4D PET* phases. The mean relative overlap among the 4 phases was equal to 88.1% for Patient 2, 90.2% for Patient 3, 89.3% for Patient 5.

Motion compensated 4D PET

A comparison with the conventional motion compensated 4D PET was performed on the 4 breathing phases of the respiratory cycle. Moreover,

for the 0% phase, each contribution to the motion compensated 4D PET

540   image was taken into consideration.

Table VI summarizes the lesion centroid localization error. As for

the *virtual 4D PET* (Table V), the maximum errors overall were comparable

to the PET and CT slice thickness.

TABLE VI

The relative overlap was calculated between the segmented lesion

volume on the 4D PET reference phase and on the motion compensated 4D

PET phase. The mean overlap among the motion compensated 4D PET

550   phases was 83.2% for Patient 2, 91.3% for Patient 3 and 89.5% for Patient

5.

Virtual 4D PET vs. Motion compensated 4D PET in patient data

As an exemplifying case for comparison between the two strategies,

Figure 6 reports, for Patient 2 (A) and Patient 3 (B), the relative

displacement in terms of Euclidean distance of lesion centroid with respect

to the mean centroid position, calculated on the real 4D PET. For Patient 2,

that displayed the highest peak to peak range of motion, lesion motion was

560   recovered within 7 mm of relative displacement.

FIGURE 6. Relative displacement with respect to the mean centroid position, for the 4D PET, the *virtual 4D PET* and the motion compensated 4D PET in Patient 2 (A) and Patient 3 (B).
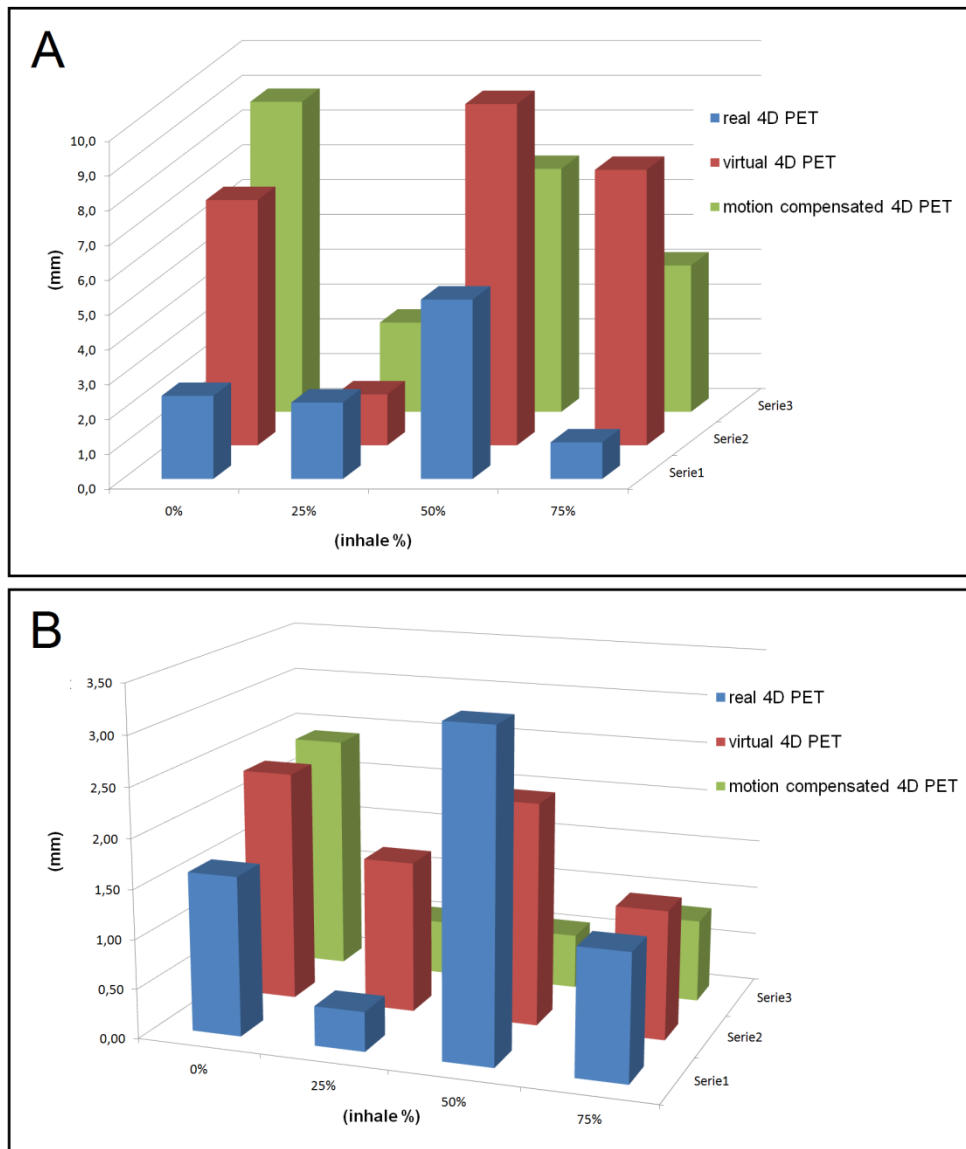
Results should be interpreted by considering that the lesion segmentation on the real 4D PET, that is the reference of the quantification, was characterized by low reliability due to noise. When lesion centroid position was compared among *virtual 4D PET* and motion compensated 4D PET for all the examined patient cases, differences were always lower than 3.16 mm in all respiratory phases.

Discussions

In this work we describe a strategy to generate 4D PET images from a free-breathing PET scan, relying on 4D CT motion modeling. The method is proposed for clinical applications where the use of hybrid CT-PET scanners is the elective imaging strategy (e.g. in radiation oncology). The proposed *virtual 4D PET* strategy aims at 4D PET optimization, with potential advantages with respect to conventional motion compensation and count statistics optimization strategies in 4D PET. The advantages can be classified as clinical, methodological and computational. From the clinical point of view, it should be noted that the *virtual 4D PET* strategy does not require PET acquisition in 4D. The PET image is acquired in free-breathing following the 4D CT session in a hybrid CT-PET scanner. This implies a simplified clinical setup, since breathing motion detection inside the PET scanner bore is not required. The image quality of the *virtual 4D PET* is

theoretically coincident to the one of a free-breathing PET image, provided

590   that the image warping process does not introduce artifacts. This permits to extend conventional PET image quality in time-resolved PET, with no need to increase the concentration of radioactive tracer administered to the patient. Also, the overall acquisition time is reduced with respect to 4D PET, and is comparable to a free-breathing PET scan. In combined 4D CT-PET treatment planning, PET contouring would be performed on the free-breathing PET. Therefore, differently from conventional motion compensated 4D PET, this approach would not introduce inaccuracies due to breathing pattern changes between the CT and PET scans. From the methodological point of view, the proposed strategy ensures a reduced

600   sensitivity to breathing pattern changes during the acquisition, if compared to conventional techniques for motion compensation in 4D PET. Although the robustness of the *virtual 4D PET* against breathing irregularities was not specifically investigated (*26*), the influence of breathing pattern changes is intrinsically limited in this strategy. A future evaluation of the increased robustness of the *virtual* 4D PET against breathing irregularities would require to consider 4D attenuation and 4D scatter corrections, since the PET activity distribution (i.e., the 4D emission map) is modified according to information coming from the CT image (i.e., the 4D attenuation map) (*27*). The issue of 4D CT motion model inaccuracies due to breathing

610   irregularities is expected to be more critical for conventional motion

compensated 4D PET. This latter method requires ideal co-registration of CT and PET images at each phase, as PET volumes are warped according to the motion model defined on the corresponding CT volume. For the *virtual 4D PET* strategy the co-registration assumption is less restrictive, because accurate co-registration is required only between the average 3D CT and 3D PET scans, and not for each corresponding phase. In terms of computational advantages, the *virtual 4D PET* strategy requires a reduced workload. Quantitatively, the workload reduction factor in terms of registration and warping steps is directly related to the number of breathing phases of the CT acquisition in 4D.

620

Despite the above mentioned potential advantages with respect to conventional motion compensation in PET imaging, there are a number of issues of the *virtual 4D PET* strategy and the reported testing, that deserve specific consideration.

The dataset used for testing consisted of 4D CT and 4D PET only. This forced us to generate a free-breathing CT and PET volumes, which was approximated by averaging and summing the original 4D CT and 4D PET datasets, respectively. The 4D CT scan was acquired according to a phase-based gating protocol, which in presence of a regular breathing pattern samples the breathing cycle uniformly over time. The same approach applied to the free-breathing may PET potentially introduce inaccuracies, which requires a specific investigation.

630

With respect to motion compensated 4D PET, the *virtual 4D PET* strategy faces the challenge to recover the 4D PET image starting from a free-breathing 3D PET. This specifically entails the achievement of two main goals:

- the recovery of lesion motion;

- the compensation of activity blurring due to motion in the free-breathing PET.

640   The NCAT phantom study demonstrated that the *virtual 4D PET* was able to recover lesion motion. Table VII summarizes the performance of the *virtual 4D PET* strategy, in comparison to conventional motion compensation. Although standard motion compensated 4D PET showed better performance overall, the *virtual 4D PET* strategy demonstrated lesion localization errors lower than 25% of the voxel size (0.38 mm) and true lesion volume estimation uncertainties below 6% (0.31 cm^3).

TABLE VII

650   Conversely, the compensation of activity blurring due to motion turned out to be more challenging, as the *virtual 4D PET* generation starts from a free-breathing, motion blurred PET. Results on the NCAT phantom demonstrated that the spill out activity was removed, but that the partial volume effect was only partially compensated (see the "Computational

anthropomorphic phantom" paragraph in the "Results" section). It should be noted that the implemented deformable registration procedure defined the deformation field, according to a pull-back warping formalism. In this case, the motion model describes the voxel intensity of the source image to be pulled onto the current voxel of the moving image. This intrinsically prevents to build up activity counts onto the current voxel: in other words the warped image cannot display a voxel intensity higher than the maximum voxel intensity of the source image. For this reason, the maximum value of the *virtual 4D PET* coincides with the 3D PET lesion peak.

A further issue is represented by the lack of inverse consistency of the adopted B-spline based deformable registration algorithm (*28*). This did not allow us to implement the *virtual 4D PET* strategy as an intra-reconstruction optimization (*29,30*), similarly to state-of-the-art motion compensation in 4D PET (*10*). Inverse consistent deformable registration algorithm (*28*) could be used to optimize the performance of the *virtual 4D PET* strategy according to the intra-reconstruction method (*31,32*).

The analysis on patient data proved the applicability of the *virtual 4D PET* strategy on clinical PET scans to optimize the count statistics, thus recovering the count statistics of the free-breathing PET. Despite the blurred activity due to motion, the lesion motion on the examined dataset could be detected with an accuracy comparable to conventional motion compensation (Table V and Table VI, Figures 5 and Figure 6). However, inaccuracies in

lesion segmentation, especially on small lesions, strongly influenced the quantification.

680 **<u>Conclusion</u>**

The proposed *virtual 4D PET* strategy showed the potential to optimize 4D PET count statistics, as equal to the free-breathing PET, with similar performance with respect to conventional motion compensation technique in 4D PET, relying on a motion model derived from 4D CT. The main advantages are related to the computational cost, the minor co-registration restrictiveness and clinical feasibility, as no 4D PET acquisition is required. The *virtual 4D PET* strategy can be employed to produce 4D PET images with a reduction in the radioactive tracer and the scan time that 690 is typically needed for 4D PET studies, provided that 4D CT data are available.

References

700

1. A. Rahmim, J. Tang, H. Zaidi. Four-Dimensional Image Reconstruction Strategies in Cardiac-Gated and Respiratory-Gated PET Imaging. *PET Clinics* **8**, 51-67 (2013). DOI: 10.1016/j.cpet.2012.10.005.

2. O.R. Mawlawi, L.E. Court. Four-Dimensional PET-CT in Radiation Oncology. *PET Clinics,* **8**(1), 81-94 (2013). DOI: 10.1016/j.cpet.2012.09.010.

3. S.C. Strother, M.E. Casey, E.J. Hoffman. Measuring PET Scanner Sensitivity: Relating Countrates to Image Signal-to-Noise Ratios using Noise Equivalent Counts. *IEEE Trans. Nucl. Sci.* **37**, 783-788 (1990). DOI: 10.1109/23.106715.

4. J.R. McClelland, D.J. Hawkes, T. Schaeffter, A.P. King. Respiratory motion models: A review. *Medical Image Analysis*, 17(1), 19-42 (2013). DOI: 10.1016/j.media.2012.09.005.

5. K.K. Brock, D.L. McShan, R.K. Ten Haken et al.. Inclusion of organ deformation in dose calculations. *Med. Phys.* **30**, 290-295 (2003). DOI: 10.1118/1.1539039.

6. M. Blume, A. Martinez-Möller, A. Keil, N. Navab, M. Rafecas. Joint Reconstruction of Image and Motion in Gated Positron-

710

720   Emission-Tomography. *IEEE Trans. Med. Imag.* **29**, 1892-1906 (2010). DOI: 10.1109/TMI.2010.2053212.

7. M. Dawood, F. Büther, X. Jiang, K.P. Schäfers. Respiratory Motion Correction in 3-D PET Data With Advanced Optical Flow Algorithms. *IEEE Trans. Med. Imag.* **27**, 1164-1175 (2008). DOI: 10.1109/TMI.2008.918321.

8. W. Bai, M. Brady. Regularized B-spline deformable registration for respiratory motion correction in PET images. *Phys. Med. Biol.* **54**(9), 2719-2736 (2009). DOI: 10.1088/0031-9155/54/9/008.

9. D. Wallach, F. Lamare, G. Kontaxakis, D. Visvikis. Super-
730   Resolution in Respiratory Synchronized Positron Emission Tomography. *IEEE Trans. Med. Imag.* **31**(2), 438-448, (2012). DOI: 10.1109/TMI.2011.2171358

10. S.A. Nehmeh. Respiratory motion correction strategies in thoracic PET-CT. *PET Clinics* **8**, 29-36 (2013). DOI:10.1016/j.cpet.2012.10.004.

11. T. Li, B. Thorndyke, E. Schreibmann, Y. Yang, L. Xing. Model-based image reconstruction for four-dimensional PET. *Med. Phys.* **33**, 1288-1298 (2006). DOI: 10.1118/1.2192581.

12. F. Lamare, M.J. Ledesma Carbayo, T. Cresson et al.. List-mode-
740   based reconstruction for respiratory motion correction in PET using

non-rigid body transformations. *Phys. Med. Biol.* **52**, 5187-5204 (2007). DOI: 10.1088/0031-9155/52/17/006.

13. J.R. McClelland, J.M. Blackall, S. Tarte et al.. A continuous 4D motion model from multiple respiratory cycles for use in lung radiotherapy. *Med. Phys.* 33, 3348-3358 (2006). DOI:10.1118/1.2222079.

14. Q. Zhang, A. Pevsner, A. Hertanto et al.. A patient-specific respiratory model of anatomical motion for radiation treatment planning. *Med. Phys.* 34, 4772-4781 (2007). DOI:10.1118/1.2804576.

15. F. Qiao, T. Pan, J.J.W. Clark, O.R. Mawlawi. A motion-incorporated reconstruction method for gated PET studies. *Phys. Med. Biol.* **51**, 3769-3783 (2006). DOI: 10.1088/0031-9155/51/15/012.

16. C. Cavedon, E. Berna, P. Francescon et al.. Building a PET time series using information from 4D CT data. *Med. Phys.* **33**, abstract 2027 (2006). DOI: 10.1118/1.2240811.

17. C. Gianoli, G. Fontana, M. Riboldi, C. Cavedon, G. Baroni. Enhanced 4D PET optimization based on 4D CT motion modeling. *ESTRO 2011 Anniversary Congress*. abstract 13022 (2011). DOI: 10.1016/S0167-8140(11)70296-1.

750

760

18. H. Zaidi, H. Vees, M. Wissmeyer. Molecular PET/CT Imaging-Guided Radiation Therapy Treatment Planning. *Academic Radiology* **16**(9), 1108-1133 (2009). DOI: 10.1016/j.acra.2009.02.014.

19. W.P. Segars. Development of a new dynamic NURBS-based cardiactorso (NCAT) phantom. Ph.D. thesis, University of North Carolina (2001).

20. J.A. Shackleford, N. Kandasamy, G.C. Sharp. On developing B-spline registration algorithms for multi-core processors. *Phys. Med. Biol.* **55**(21), 6329-6351 (2010). DOI: 10.1088/0031-9155/55/21/001.

21. E. De Bernardi, M. Mazzoli, F. Zito, G. Baselli. Resolution Recovery in PET During AWOSEM Reconstruction: A Performance Evaluation Study. *IEEE Trans. Nucl. Sci.* **54**, 1626-1638 (2007). DOI: 10.1109/TNS.2007.905167.

22. H.M. Hudson, R.S. Larkin. Accelerated Image Reconstruction Using Ordered Subsets of Projection Data. *IEEE Trans. Med. Imag.* **13**, 601-609 (1994). DOI: 10.1109/42.363108.

23. Z. Hu, W. Wang, E.E. Gualtieri et al.. An LOR-based fully-3D PET image reconstruction using a blob-basis function. *IEEE Nuclear Science Symp. Conf. Rec.* **6**, 4415-4418 (2007). DOI: 10.1109/NSSMIC.2007.4437091.

770

780

24. M. MacManus, U. Nestle, K.E. Rosenzweig et al.. Use of PET and PET/CT for radiation therapy planning: IAEA expert report 2006-2007. *Radiother. Oncol.* **91**, 85-94 (2009). DOI: 10.1016/j.radonc.2008.11.008.

25. Y.E. Erdi, O. Mawlawi, S.M. Larson et al.. Segmentation of Lung Lesion Volume by Adaptive Positron Emission Tomography Image Thresholding. *Cancer* **80**, 2502-2509 (1997). DOI: 10.1002/(SICI)1097-0142.

26. A.P. King, C. Buerger, C. Tsoumpas, P.K. Marsden, T. Schaeffter. Thoracic respiratory motion estimation from MRI using a statistical model and a 2-D image navigator. *Medical Image Analysis*, **16**(1), 252-264 (2012). DOI: 10.1016/j.media.2011.08.003.

27. H.J.Fayad, F. Lamare, C. Cheze Le Rest et al.. Generation of 4-Dimensional CT Images Based on 4-Dimensional PET–Derived Motion Fields. *J. Nucl. Med.* 54(4), 631-638 (2013). DOI: 10.2967/jnumed.112.110809.

28. E.T. Bender, W.A. Tomé. The utilization of consistency metrics for error analysis in deformable image registration. *Phys. Med. Biol.* **54**(18), 5561-5577 (2009). DOI: 10.1088/0031-9155/54/18/014.

29. I. Polycarpou, C. Tsoumpas, P. K. Marsden. Analysis and comparison of two methods for motion correction in PET imaging. *Med. Phys.* **39**(10), 6474-6483 (2012), DOI: 10.1118/1.4754586.

790

800

30. N. Dikaios, T.D. Fryer. Improved motion-compensated image reconstruction for PET using sensitivity correction per respiratory gate and an approximate tube-of-response backprojector. *Med. Phys.* **38**(9), 4958-4970 (2011). DOI: 10.1118/1.3611041

810   31. S.Y. Chun., J.A. Fessler. Noise Properties of Motion-Compensated Tomographic Image Reconstruction Methods. *IEEE Trans. Med. Imag.* **32**(2), 141-152 (2013). DOI: 10.1109/TMI.2012.2206604.

32. C. Tsoumpas, I. Polycarpou, K. Thielemans et al.. The effect of regularization in motion compensated PET image reconstruction: a realistic numerical 4D simulation study. *Phys. Med. Biol.* **58**(6), 1759- 1773 (2013). DOI:10.1088/0031-9155/58/6/1759.

Tables

820   TABLE I. Deformable registration parameters for each multi-resolution stage.

	B-spline grid spacing (mm)		Resolution (voxels)		Number of iterations
	Trans-axial	**Axial**	**Trans-axial**	**axial**	
Stage 1	60	60	2	2	40
Stage 2	40	40	2	2	20
Stage 3	30	20	1	1	20
Stage 4	15	10	1	1	20

TABLE II. Features of the 4D CT-PET NCAT dataset.

Breathing motion parameters		
Phases per breathing cycle	10	
Peak to peak breathing motion amplitude(cm)	SI diaphragm motion	2
	AP chest wall expansion	1.2
Image parameters		
Voxel dimension (mm³)	$1,5 \times 1,5 \times 1,5$	
Image dimension (voxels)	$256 \times 256 \times 200$	

TABLE III. Features of the clinical dataset.

	Voxel dimension (mm)		Image dimension (voxels)		Lesion position
	CT	**PET**	**CT**	**PET**	
Patient 1	$1.1719 \times 1.1719 \times 3$	$4 \times 4 \times 4$	$512 \times 512 \times 144$	$144 \times 144 \times 107$	Upper-posterior part of left lung
Patient 2	$1.1719 \times 1.1719 \times 3$	$4 \times 4 \times 4$	$512 \times 512 \times 53$	$144 \times 144 \times 66$	Lower-middle part of right lung
Patient 3	$0.7813 \times 0.7813 \times 5$	$4 \times 4 \times 4$	$512 \times 512 \times 36$	$144 \times 144 \times 45$	Lower-posterior part of left lung
Patient 4	$1.1719 \times 1.1719 \times 5$	$4 \times 4 \times 4$	$512 \times 512 \times 36$	$144 \times 144 \times 45$	Central-posterior part of left lung
Patient 5	$1.1719 \times 1.1719 \times 5$	$4 \times 4 \times 4$	$512 \times 512 \times 36$	$144 \times 144 \times 45$	Liver
Patient 6	$1.1719 \times 1.1719 \times 3$	$4 \times 4 \times 4$	$512 \times 512 \times 59$	$144 \times 144 \times 45$	Central-posterior part of left lung / Lower-posterior part of right lung / Upper-middle part of the right lung
Patient 7	$1.1719 \times 1.1719 \times 5$	$4 \times 4 \times 4$	$512 \times 512 \times 36$	$144 \times 144 \times 45$	Upper/middle part of left lung / Central-posterior part of left lung

830   TABLE IV. Lesion range of motion.

	4D CT range of motion (mm)	**4D PET range of motion (mm)**
Patient 1	1.19	0.93
Patient 2	18.43	7.54
Patient 3	13.48	4.88
Patient 4	0.91	2.01
Patient 5	1.52	7.66
Patient 6	0.87	0.65
	0.43	0.92
	0.52	1.36
Patient 7	0.99	1.50
	0.55	2.02

TABLE V. Lesion centroid localization error: *virtual 4D PET*.

	CT centroid localization (mm)		PET centroid localization (mm)	
	4D CT phases		**4D PET phases**	
	Mean error	Maximum error	Mean error	Maximum error
Patient 1	0.08	0.09	0.48	0.56
Patient 2	1.41	2.00	3.45	6.53
Patient 3	0.71	1.18	1.56	3.08
Patient 4	0.77	0.88	1.41	1.63
Patient 5	1.29	1.94	3.28	6.12
Patient 6	0.25	0.44	1.37	2.71
	0.15	0.29	2.21	6.24
	0.26	0.36	3.73	9.51
Patient 7	0.19	0.33	1.66	2.96
	0.12	0.21	0.97	1.99

TABLE VI. Lesion centroid localization error: motion compensated 4D

PET. For the motion compensated phase, the mean and the maximum errors

840   are referred to 4D CT and 4D PET contributions, respectively.

	CT centroid localization (mm)				PET centroid localization (mm)			
	4D CT phases		**Motion compensated 0% phase**		**4D PET phases**		**Motion compensated 0% phase**	
	Mean error	Maximum error	Mean error	Maximum error	Mean error	Maximum error	Mean error	Maximum error
Patient 1	0.32	1.14	0.10	0.16	0.60	0.92	0.46	0.69
Patient 2	1.47	0.72	0.98	0.94	4.79	8.59	7.57	14.97
Patient 3	0.83	1.51	1.78	2.57	2.06	2.73	2.60	4.18
Patient 4	0.45	0.62	1.27	2.07	1.55	1.99	1.46	2.40
Patient 5	1.09	1.77	0.72	1.40	3.68	5.31	5.56	7.92
Patient 6	0.14	0.21	0.17	0.31	1.26	2.71	1.50	2.14
	0.28	0.48	1.24	1.67	2.22	6.31	2.75	8.95
	0.26	0.37	0.26	0.58	3.52	9.63	3.85	10.20
Patient 7	0.48	0.75	0.19	0.30	1.65	2.58	1.59	3.88
	0.09	0.17	0.08	0.19	1.17	1.86	0.93	1.60

TABLE VII. General comparison between the motion compensated 4D PET

and *virtual 4D PET* strategies for the NCAT phantom.

	Centroid localization error (mm)	Relative overlap (% with respect the corresponding 4D PET phase)
Motion compensated 4D PET (0% phase)	0.049	98.8%
Virtual 4D PET	0.370	94.2%